Multi-scale analysis of thermoelastic properties of graphene foam/PDMS composites

Multi-Scale Analysis of Thermoelastic Properties of Graphene Foam/Polymer Composites

Sajedeh Khosravani[a,b], Mohammad Homayoune Sadr[a,*], Erasmo Carrera[b], Alfonso Pagani[b], and Alberto Racionero Sanchez-Majano[b]

[a]*Department of Aerospace Engineering, Amirkabir University of Technology (Tehran Polytechnic), Tehran, Iran*
[b]*Department of Mechanical and Aerospace Engineering, Politecnico di Torino, Turin, Italy*

Abstract

In macroscopic applications, the production of graphene foam (GF) can be an attractive way to utilize the combined advantages of graphene sheets and porous materials. The porosity level significantly affects mechanical and thermal properties by changing the specific surface area. In this study, a multi-scale method is used to calculate the coefficient of thermal expansion (CTE) and heat capacity of GF/polymer composites. Molecular dynamics have calculated the properties of 3D GFs. In particular, four types of GF with increasing mass density and decreasing porosity are investigated. The thermoelastic properties are calculated as temperature-dependent for all groups of GF. Mechanics of structure genome (MSG) based on Carrera unified formulation (CUF) is used to calculate the effective properties of the GF/polymer composites. It was found that the composite consisting of GF with the highest density and lowest porosity has the minimum CTE. Also, the heat capacity of the composite depends not only on the heat capacity of the components but also on their Young modulus, CTE, and geometry.

Keywords:
Graphene foam, CTE, Specific heat, LAMMPS software, CUF micro-thermoelastic model, Multi-scale modeling.

1. Introduction

Recently, graphene has attracted a great deal of attention in thermal applications. In the last decade, there has been a lot of use of graphite and graphene sheets as reinforcements for polymer composites. Graphene sheets tend to accumulate due to strong van der Waals forces. Therefore, by dispersion them in polymer matrices, the phenomenon of agglomeration occurs, and the synergistic effects are not achieved. This is why the use of graphene in macro dimensions is always a challenge. Researchers have proposed many solutions to solve the problem of graphene dispersion in polymer matrices. Meanwhile, among them, the best solution is to create a three-dimensional (3D) bond between the graphene sheets and use it as a 3D graphene foam (GF) [1]. GF is one of the carbon foam structures that consists of nanosheets of graphene

*Corresponding author.
Email address: sadr@aut.ac.ir (Mohammad Homayoune Sadr)

and a large number of pores. Due to its networked structure, this material has properties such as a high specific surface area, lightweight, high-temperature stability, excellent electrical and thermal conductivity, and high mechanical properties. For this reason, many different methods have been used to calculate the properties of this type of material in research work. Lin et al. [2] conducted a study on thermal diffusivity suspended GF using the transient electro heat method. The results of their research express that the inherent thermal conductivity (TC) of suspended GF is lower than those presented for single-layer graphene. GF structural defects observed by them explained the significant reduction in TC. Jia et al. [3] produced GF/epoxy nanocomposites using the chemical vapor deposition method. They found in experiments that 3D GF grids act as fast carriers for load transfer. Li et al. [4] showed that thermal properties of GFs increase with a temperature above 25 °C. Their study marked a significant increase in TC and thermal diffusivity for GF. Zhao et al. [5] fabricated polymer composites consisting of GF, graphene sheets, and Polydimethylsiloxane (PDMS) and analyzed their TC and the coefficient of thermal expansion (CTE). They compared GF/PDMS thermal properties with composites containing graphene sheets and proved the superiority of GF composite. Zhao et al. [6] investigated the effect of carbon fiber on the mechanical and thermal properties of GF/carbon fiber/PDMS composites through the different volume fractions of GF in the PDMS matrix. Zhang et al. [7] studied the thermal behavior of a polymer composite filled with GF using finite element method (FEM). It has been shown that the thermal conductance of interfacial between GF and the PDMS matrix has a minimal effect on the TC of the composite. Sadr and Vahedi [8] calculated the TC of graphene/hexagonal-boron nitride structures; in the first step by simulating molecular dynamics (MD), they examined the polycrystalline film with nano-sized particles at the atomic scale. Then, using the atomic scale results, they developed a model by FEM for the macro-scale material to determine heat conduction. Menci and Kirka [9] scrutinized the thermal properties of GFs with and without fullerene by performing reverse non-equilibrium molecular dynamics (RNEMD) simulations. On the other hand, achieving the GF properties with the MD approach, although it can fully simulate atomic interactions, the results can only be compared with nanoscale results. Therefore, a multi-scale approach is ideal for GFs, which have an intrinsic multi-scale property due to their micron-sized pores. In the new simulation techniques, the major challenge in the problems is various scales, which can be remarkably reduced by using multi-scale modeling techniques. In multi-scale processes, properties can be related to different scales by several computational steps. Micromechanical modeling methods are effective tools for understanding how the reinforcement affects the macroscopic composite. In this field of research, several analytical and numerical methods have been presented, such as mathematical homogeneity theories (MHT) [10], finite element approaches using analysis of representative volume element (RVE) [11], and many others. In the present study, mechanics of structure genome (MSG) [12] is used to solve the repeating unit cell (RUC) problem using a new 1D approach. Also, Carrera unified formulation (CUF) [13] is employed as a high-precision tool to reduce 3D structural problems to 1D models [14] or 2D models [15]. From this perspective, the limitations of the classical theories of beams and plates/shells are removed using the desired kinematic correction and expression of the governing equations in a hierarchical manner. Using these capabilities, the RUC can be modeled using beam elements along the fiber direction and non-local expansion of unknown variables in the other two directions [16]. The effective thermal properties of composites are influenced by parameters such as volume fraction, topology, and properties of components. In addition, the use of temperature-dependent thermoelastic properties such as CTE, TC, Young modulus, and Poisson ratio based on CUF, increases the accuracy of calculations [17]. It is worth noting that calculating thermal properties such as CTE and specific heat as temperature-dependent values are

essential for electronics and heating systems applications which is calculated in this work. The present work is organized as follows: First, the atomic modeling of the GF structures and calculation of CTE and specific heat through the MD approach is described in section 2. Then section 3 explains the micro-thermoelastic CUF approach for the computation of effective properties. Finally; in section 4 and section 5, the result and conclusions are presented, respectively.

2. Atomistic Modeling and Simulation Details

In this study, irregular GF is simulated using dispersion graphene sheets in a polycrystalline substrate by the large-scale atomic/molecular massively parallel simulator (LAMMPS) package[18]. The MD simulation process is briefly shown in Fig. 1. First, a polycrystalline box of the face-centred cubic (FCC) Au (lattice size equal to 0.4065 nm) is grained by Atomsk software [19], and some grains are removed randomly, Fig. 1(a) and 1(b). Then a graphene monolayer with a length along x and y equal to 0.5 nm is simulated. The simulated monolayers are randomly distributed among the polycrystalline grains by developing a python code, Fig 1(c). The mass density of GF simulated depends on the number of polycrystalline grains that remained in the box and the number of graphene monolayers dispersed among them. Next, the AIREBO potential [20] is adjusted between carbon atoms by simulating in atomic phase and periodic boundary conditions. It should be noted that there is no chemical bond between the graphene sheets and the Au atoms, and they are connected using a Lennard-Jones (L-J) potential. Finally, GF is formed under the following conditions: a simulation box consisting of 24,000 carbon atoms in the form of graphene sheets placed among Au polycrystals. The carbon-carbon bond length in this simulation is 0.1418 nm. L-J parameters are calculated between carbon and Au atoms using the Lorentz-Berthelot mixing rules [21]. The simulation box pressure increases from 1 atm to 1000 atm under a temperature of 300 K and uses the isothermal-isobaric NPT ensemble and stabilized at a pressure of 1000 atm. Also, the temperature increased from 300 K to 3000 K, and then its equilibrium at 3000 K by applying the canonical NVT ensemble. Then the temperature decreases again from 3000 K to 300 K, and this heating and cooling cycle is repeated four times so that the carbon atoms have enough time to form a bond. The size of the simulation boxes in the three directions x, y, and z is equal to $80 \times 80 \times 80\,\text{Å}^3$. This simulation is performed in each stage for 100 ps with a time step of 0.001 ps. The stable structure of GF is achieved by removing the polycrystal grains and equilibrating it, shown in Fig. 1(d). Molecular visualization in this work is represented by the OVITO package [22].

2.1. Coefficient of Thermal Expansion

The CTE, which measures the change in length, area, or volume of a material with increasing temperature, is an essential parameter for many applications. Although the design of materials with a controlled CTE is crucial today, there is no precise approach to achieving this parameter in GF materials.

In this study, MD simulations are performed in order to calculate the CTE of GF by defining carbon atoms in a cubic region. The AIREBO potential has been used to express the interactions of carbon atoms. The periodic boundary condition is applied in all three directions, and the time step for the simulation is set to 0.001 ps. As the first step, the system temperature is equilibrated under the NVT ensemble at 300 K in 100 ps. In the next step, under constant pressure, the system's temperature is increased from 300 K to 700 K and by using the NPT ensemble equilibrated at 700 K. The simulation is repeated 6 million times by selecting the appropriate damping

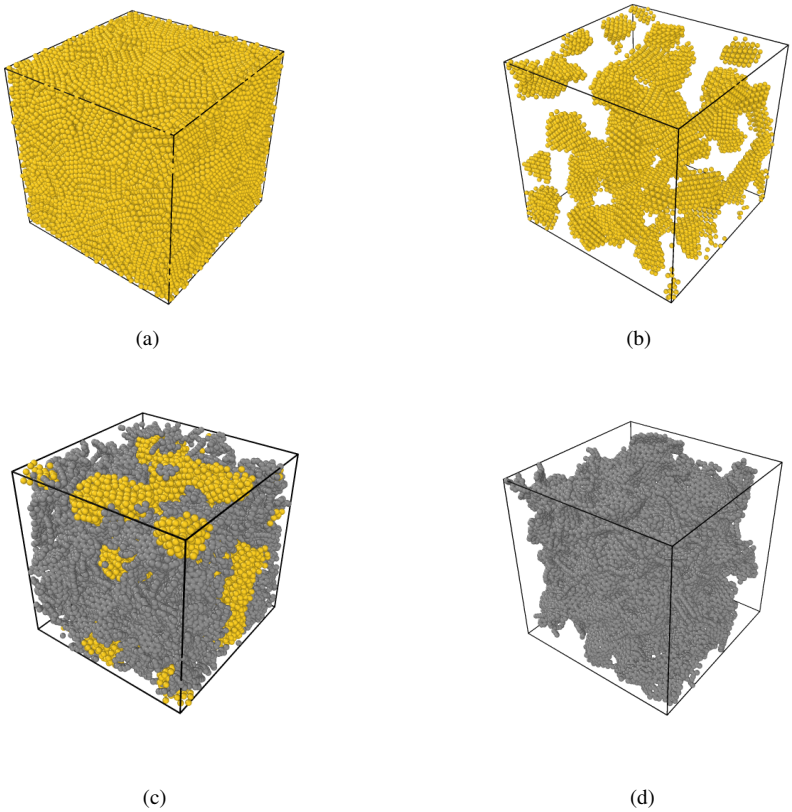

Figure 1: The simulation steps for generated GF, (a) The polycrystalline metal lattice is shown to be regular, (b) Several polycrystalline grains by randomization have been removed, (c) Graphene sheets are distributed among the polycrystalline grains and removed if they are too close to the polycrystalline atoms, (d) After heating and cooling cycles, polycrystalline grains are removed and created GF.

parameter in each stage. The whole system's pressure, temperature, and energy parameters are controlled during this process. Finally, the axial CTE of GFs for each temperature is calculated using the following formulation.

$$\alpha(T) = \frac{dL}{dT} \cdot \frac{1}{L} \tag{1}$$

where the expression dL/dT is equal to the slope of variation of length with increasing temperature, and L is the initial length of the simulation box in different directions. It should be noted that the initial length L of the simulation box is at a temperature of 300 K. In order to calculate the CTE, the heating temperature of the system has been converted to linear intervals. In other words, the temperature range between 300 K to 700 K is divided into 20 temperature ranges of 20 K. During the simulation, by heating the system, the length of the simulation box is measured

at different temperatures in three directions x, y, and z.

2.2. Specific Heat

Several methods of calculating specific heat exist, some of which have an independent temperature and others dependent. In the present study, the calculation of specific heat of GF has been investigated using a formula based on statistical mechanics [23]. Calculating specific heat is the same as calculating the CTE, except that the specific heat is calculated in thermal equilibrium cycles at different temperatures. The NVT ensemble and Nose-Hoover thermostat are applied to achieve equilibrium of simulated GF in the specific heat measurement in the MD platform. Internal energy, enthalpy, temperature, and system's pressure continuously are measured during the simulation. It is worth mentioning that the specific heat in this simulation is specific heat of isochoric ($c_v = (\partial U/\partial T)_V$). The isochoric specific heat can be calculated as:

$$c_v = \frac{< U^2 > - < U >^2}{k_B T^2 m} \tag{2}$$

in which U, T, and m are the system's internal energy, temperature, and total mass. k_B is Boltzmann constant, and $< ... >$ represents the mean of the variable [24]. There is no doubt that by multiplying the density by the specific heat, heat capacity is obtained.

3. Micro-Thermoelastic CUF Method

This work employs an efficient thermoelastic micromechanical model for the prediction of purely elastic properties (Young modulus and Poisson ratio), as well as thermal properties, such as CTE and specific heat at constant volume. The proposed model assumes that the arrangement of the constituents follows a periodic pattern named RUC, which represents the minimum geometrical building block that can be repeated over the space to shape the material's higher scales, Fig. 2. Additionally, the following two assumptions are made:

- The local solutions have an average value over the RUC volume that is equal to the global solution of the larger scales problem. Applying this to a field ϕ, this assumption reads as:

$$\bar{\phi}(\mathbf{x}) = \frac{1}{V}\int_V \phi(\mathbf{x};\mathbf{y})dV \tag{3}$$

  in which $\mathbf{x}$ and $\mathbf{y}$ denote the global and RUC's local reference system, respectively.

- The effective material properties obtained from the RUC analyses do not depend on the loading and boundary conditions nor the geometry of the higher scales problem.

Once considered these hypotheses, the MSG is depicted. MSG, first introduced by Yu [12], exploits the variational asymptotic method (VAM) [25] for solving problems that involve smaller parameters. MSG proposes that the solution of the stationary value problem is obtained by minimising the difference between the strain energy of the heterogeneous material and that of the homogenised material. It is expressed in the following functional:

$$\Phi = \frac{1}{2}\left\langle C_{ijkl}\varepsilon_{ij}\varepsilon_{kl} + 2\beta_{ij}\varepsilon_{ij}\theta + c_v\frac{\theta^2}{T_0}\right\rangle - \frac{1}{2}\left(C^*_{ijkl}\bar{\varepsilon}_{ij}\bar{\varepsilon}_{kl} + 2\beta^*_{ij}\bar{\varepsilon}_{ij}\theta + c^*_v\frac{\theta^2}{T_0}\right) \tag{4}$$

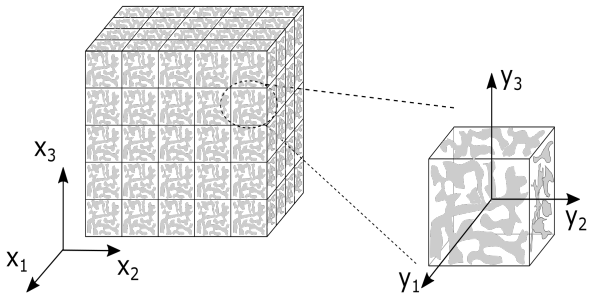

Figure 2: Coordinate reference systems of a periodic heterogeneous material and its RUC.

where $\langle\rangle$ denotes the volume average. The first term of the functional is the strain energy of the heterogeneous material represented by the RUC, whereas the second is that of the equivalent homogenised material. C_{ijkl} is the fourth-order elastic tensor, ε_{ij} and β_{ij} are the second-order strain and thermal stress tensors, respectively; c_v is the heat capacity; T_0 is the reference temperature at which the constituent material is stress-free, and θ represents the difference between the current temperature and the reference temperature.

For the sake of brevity, the derivation of how fluctuation variables ($\boldsymbol{\chi}$) are considered and how they are used for the derivation of the functional that is minimised is omitted in this manuscript, but it can be found in the works by Yu and Tang [26], de Miguel *et al.*[27], and Sanchez-Majano *et al.* [28]. Finally, the functional that MSG minimises is:

$$\Phi^* = \frac{1}{2}\langle C_{ijkl}\left[\bar{\varepsilon}_{ij} + \chi_{(i,j)}\right]\left[\bar{\varepsilon}_{kl} + \chi_{(k,l)}\right] + 2\beta_{ij}\left[\bar{\varepsilon}_{ij} + \chi_{(i,j)}\right]\theta + c_v\frac{\theta^2}{T_0}\rangle \tag{5}$$

in which $\bar{\varepsilon}_{ij} = \langle\varepsilon_{ij}\rangle$, and $\chi_{(i,j)}$ are the derivatives of the i^{th} fluctuation component with respect to the j^{th} coordinate of the RUC's local reference system $\mathbf{y}$. For further insight, the reader is referred to the aforementioned references.

The MSG problem is solved by means of the well-known CUF. Classically, CUF has been used to solve structural problems by expressing the field of displacement in terms of arbitrary expansion functions (F_τ) and generalised displacements, commonly denoted as $\mathbf{u}_\tau$. Nevertheless, the field of displacements can be substituted by the fluctuation unknowns with no further implications as follows:

$$\boldsymbol{\chi}(\mathbf{x}; y_1, y_2, y_3) = F_\tau(y_2, y_3)\boldsymbol{\chi}_\tau(\mathbf{x}; y_1) \quad \tau = 1, ..., M \tag{6}$$

in which τ denotes summation, and M is the number of expansion terms assumed in the kinematic model. In this work, hierarchical Legendre expansions (HLE) [29] are used as expansion functions and are coupled with the blending function method in order to achieve a geometrically exact representation of the RUC, as presented in [27, 30]. Finally, FEM is used to write the generalised fluctuation unknowns $\boldsymbol{\chi}_\tau$ in terms of the Lagrange shape functions N_i on the y_1 direction as:

$$\boldsymbol{\chi}_\tau(\mathbf{x}; y_1) = N_i(y_1)\boldsymbol{\chi}_{\tau i}(\mathbf{x}) \quad i = 1, ..., N \tag{7}$$

where $\boldsymbol{\chi}_{\tau i}(\mathbf{x})$ is the nodal unknown vector and N is the total number of beam nodes. The geometrical relations can be written as:

$$\varepsilon = \bar{\varepsilon} + \mathbf{D}\boldsymbol{\chi} \tag{8}$$

in which $\mathbf{D}$ is the differential operator that relates strains and displacements. Then, substituting Eq. (8) in the functional from Eq. (5), one gets the following expression for the functional:

$$\Phi^* = \frac{1}{2}\int_V \left[(\bar{\varepsilon} + \mathbf{D}\boldsymbol{\chi})^T \mathbf{C} (\bar{\varepsilon} + \mathbf{D}\boldsymbol{\chi}) + 2\beta(\bar{\varepsilon} + \mathbf{D}\boldsymbol{\chi})\theta + c_v \frac{\theta^2}{T_0} \right] dV \tag{9}$$

Then, introducing Eq. (7) into Eq. (6), and the latter in Eq. (9), the functional Φ^* reads in CUF form as:

$$\Phi^* = \frac{1}{2}\left(\boldsymbol{\chi}_{sj}^T \boldsymbol{E}^{\tau sij} \boldsymbol{\chi}_{\tau i} + 2\boldsymbol{\chi}_{sj}^T \boldsymbol{D}_{h\varepsilon}^{sj} \bar{\boldsymbol{\varepsilon}} + \bar{\boldsymbol{\varepsilon}}^T \boldsymbol{D}_{\varepsilon\varepsilon} \bar{\boldsymbol{\varepsilon}} + 2\boldsymbol{\chi}_{sj}^T \boldsymbol{D}_{h\theta}^{sj} \theta + 2\bar{\boldsymbol{\varepsilon}}^T \boldsymbol{D}_{\varepsilon\theta} \theta + D_{\theta\theta} \frac{\theta^2}{T_0} \right) \tag{10}$$

where

$$\begin{gathered} \mathbf{E}^{\tau sij} = \int_\Omega \int_l (\boldsymbol{D}(F_\tau N_i \boldsymbol{I}))^T \boldsymbol{C} \boldsymbol{D}(F_s N_j \boldsymbol{I}) d\Omega dy_1 \qquad \mathbf{D}_{h\varepsilon}^{sj} = \int_\Omega \int_l (\boldsymbol{D}(F_s N_j \boldsymbol{I}))^T \boldsymbol{C} d\Omega dy_1 \\ \mathbf{D}_{\varepsilon\varepsilon} = \int_V \boldsymbol{C} dV \qquad \mathbf{D}_{h\theta}^{sj} = \int_\Omega \int_l (\boldsymbol{D}(F_\tau N_i \boldsymbol{I}))^T \boldsymbol{\beta} d\Omega dy_1 \qquad \mathbf{D}_{\varepsilon\theta} = \int_V \beta dV \qquad \mathbf{D}_{\theta\theta} = \int_V c_v dV \end{gathered} \tag{11}$$

$\mathbf{I}$ is the 3×3 identity matrix. On one side, $\mathbf{E}^{\tau sij}$, $\mathbf{D}_{h\varepsilon}^{sj}$, $\mathbf{D}_{h\theta}^{sj}$ are the fundamental nuclei of the RUC problem, containing all the structural model information. On the other side, $\mathbf{D}_{\varepsilon\varepsilon}$, $\mathbf{D}_{\varepsilon\theta}$ and $\mathbf{D}_{\theta\theta}$ are the averaged stiffness matrix, averaged thermal stiffness matrix and averaged heat capacity of the material, respectively. Clearly, $\mathbf{C}$ represents the 6×6 material matrix condensed from the fourth-order elastic tensor C_{ijkl}, and $\boldsymbol{\beta} = -\boldsymbol{C}\boldsymbol{\alpha}$ is the 6×1 column condensed matrix from β_{ij} and $\boldsymbol{\alpha}$ is the 6×1 array containing the CTEs. Finally, the fluctuation unknowns that minimise the previous functional can be calculated by solving the linear system:

$$\mathbf{E}\boldsymbol{\chi} = -\mathbf{D}_{h\varepsilon}\bar{\boldsymbol{\varepsilon}} - \mathbf{D}_{h\theta}\theta \tag{12}$$

Besides, assuming that the fluctuation is linearly proportional to $\bar{\boldsymbol{\varepsilon}}$ and θ, i.e.:

$$\boldsymbol{\chi} = \boldsymbol{\chi}_0 \bar{\boldsymbol{\varepsilon}} + \boldsymbol{\chi}_\theta \theta \tag{13}$$

and substituting it in Eq. (12), one can write this linear system:

$$\begin{cases} \mathbf{E}\boldsymbol{\chi}_0 = -\mathbf{D}_{h\varepsilon} \\ \mathbf{E}\boldsymbol{\chi}_\theta = -\mathbf{D}_{h\theta} \end{cases} \tag{14}$$

Finally, substituting Eq. (13) in the functional from Eq. (10), one can calculate:

$$\Phi^* = \frac{1}{2}\bar{\boldsymbol{\varepsilon}}^T \boldsymbol{C}^* \boldsymbol{\varepsilon} + \bar{\boldsymbol{\varepsilon}}^T \bar{\boldsymbol{\beta}} \theta + \frac{1}{2}\bar{c_v} \frac{\theta^2}{T_0} \tag{15}$$

with

$$\boldsymbol{C}^* = \frac{1}{\Omega}(\boldsymbol{\chi}_0^T \boldsymbol{D}_{h\varepsilon} + \boldsymbol{D}_{\varepsilon\varepsilon}) \qquad \bar{\boldsymbol{\beta}} = \frac{1}{\Omega}\left[\frac{1}{2}(\boldsymbol{D}_{h\varepsilon}^T \boldsymbol{\chi}_\theta + \boldsymbol{\chi}_0^T \boldsymbol{D}_{h\theta}) + \boldsymbol{D}_{\varepsilon\theta} \right] \qquad \bar{c_v} = \frac{1}{\Omega}[\boldsymbol{\chi}_\theta^T \boldsymbol{D}_{h\theta} T_0 + \boldsymbol{D}_{\theta\theta}] \tag{16}$$

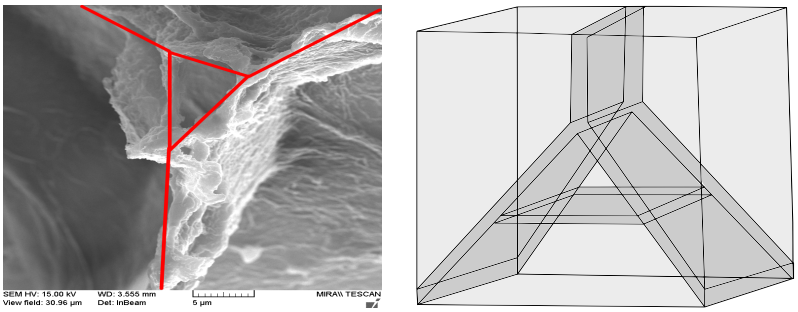

(a) (b)

Figure 3: (a) SEM image of GF [21], (b) Schematic model of the UC consists of GF (gray parts) and matrix (light gray parts).

in which $\mathbf{C}^*$ is the effective elastic coefficients matrix of the equivalent material, $\bar{\beta}$ comprises the thermal stress coefficients and $\bar{c_v}$ is the effective heat capacity. It is clear that the effective thermal expansion coefficients can be computed as: $\bar{\alpha} = -\boldsymbol{C}^{*-1}\bar{\beta}$. The similarities of the repeating components in the Scanning electron microscope (SEM) images of synthesized GF [21] allows the selection of a micro-scale unit cell (UC) with the characteristics of the whole GF. The proposed UC should have a general shape that can find itself or similar cells in any part of the synthesized GF. The cell size is unit, and its properties are obtained from MD simulation. It should be noted that the dimensions of the RUC at this stage are completely dependent on the density and volume fraction of GF. SEM image in comparison with the RUC model simulated is shown in Fig. 3. The red lines in Fig. 3(a) demonstrate the boundaries of the proposed UC. Due to SEM images being 2D, the extracted borders are only on one surface of the cubic UC. Hence, the prepared surface is extruded in the third direction to create a cubic shape. And Fig. 3(b) shows the proposed UC consists of two components: matrix and GF. The RUC of GF/polymer composite is considered with a volume fraction of 8.1% of GF and periodic boundary conditions.

4. Result and discussion

This study uses a multi-scale method to achieve the elastic and thermoelastic properties of GF reinforced composites. In this regard, four types of GF with different densities and porosity percentages are simulated to calculate their properties, see Table 1. The validity of the initial structures obtained from GF is ensured using criteria of density, radial distribution functions (RDF), number of carbon-carbon (C-C) bonds, and pore size distribution (PSD). Figure 4(a) shows the RDF diagram for the simulated GFs at the end of three heating and cooling cycles plus the pre-heating and cooling cycle. As illustrated, the first peak occurred at 1.42 Å, i.e., the C-C bond length in the graphene sheets. This peak intensity increases with each cycle which can also be seen in the C-C bond diagram. Figure 4(b) shows the actual number of C-C bonds per the number of atoms in each cycle. This bond number increases as the cycles increase to approximately converge with the number of bonds in ideal graphene (i.e., 1.5 per atom). In this study, distance criterion for two carbon atoms is lower than 1.6 Å for calculating the number of covalent bonds.

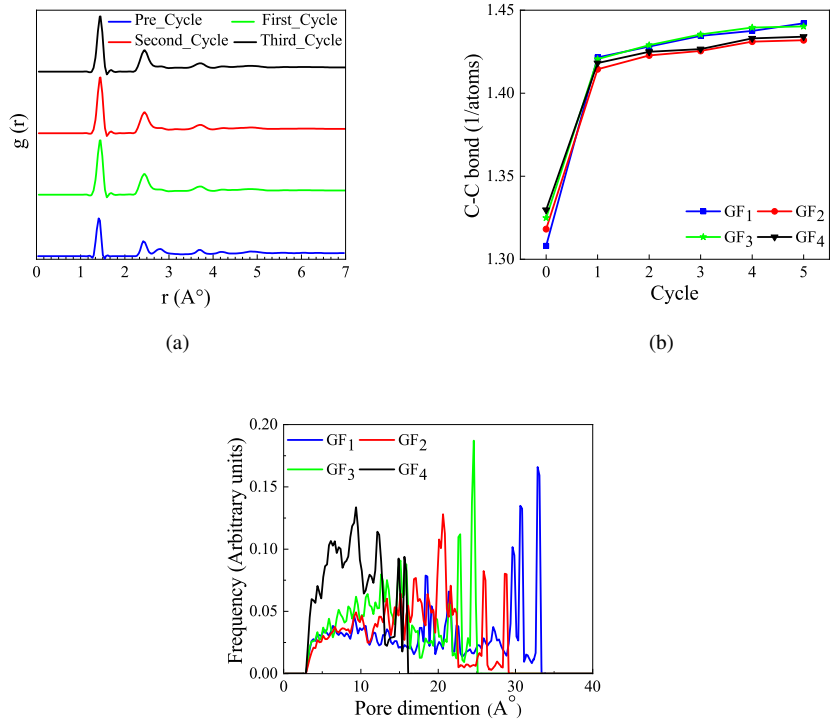

Figure 4: (a) Radial distribution functions related to heating/cooling cycles of the system, (b) The total number of covalent bonds per number of atoms at the end of each cycle, and (c) Pore size distribution for all groups of GF.

Geometric analysis of GFs and their porosity are performed using the PoreBlazer code [31]. The pore size in GFs structure can be obtained using the PSD, which is the same as the rate of absorption and desorption of gases in the laboratory method. PSD analysis provides a numerical description of the pore size range in samples. The PSDs for GF types are shown in Fig. 4(c). In this work, the specific surface area of GF has been calculated in reference to its excellent surface properties due to the 3D bonds. The PSD measurements provide a numerical description of average pore dimension, porosity percentage, and specific surface area, which is given in Table 1 for all groups of GFs. Indeed, as displayed by the PSD diagram, the pore size is approximately in the range of 0.5 nm to 3 nm. The mass densities range for GFs is between 0.5 - 0.8 (g/cm^3), which is shown in Fig. 5(a) the relation between it and average pore dimensions. And also, Fig. 5(b) shows the mass density graph versus the samples' specific surface area. As can be seen, both the pore size and the specific surface area decrease with increasing density. The high specific surface area in the low mass creates enough space for electrochemical and thermal reactions, which increases the capacity of electrical devices. With the decreasing porosity, the specific surface area is reduced, too. Actually, in GFs, energy can be stored more efficiently due

to their low mass and high specific surface area. The PSD diagrams of the simulated GFs are compared with the experimental samples from references [21, 32], and a good agreement can be appreciated. Figure 6 shows a representative piece of the same size for each of the foam types that the percentage of porosity decreases from Fig. 6(a) to Fig. 6(d), and the mass density increases. The topology of the samples simulated in this study is similar to the SEM image shown in Fig.7. Of course, it should be noted that the pore size in laboratory samples is much larger, about a few micrometers.

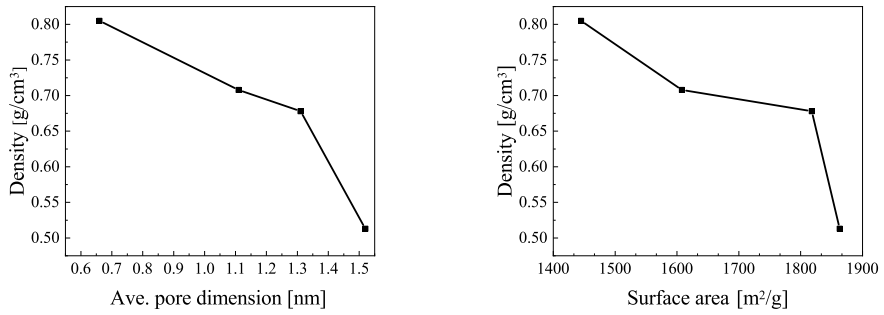

Figure 5: (a) The diagram of density versus average pore size and (b) Specific surface area for the GF samples.

Table 1: Parameters describing the four groups of GF scrutinized in this study.

Sample	Density (g/cm^3)	Porosity (%)	Avarage pore size (nm)	Surface area (m^2/g)
GF_1	0.513	78	1.52	1863
GF_2	0.678	70	1.31	1818
GF_3	0.708	66	1.11	1608
GF_4	0.805	63	0.66	1445

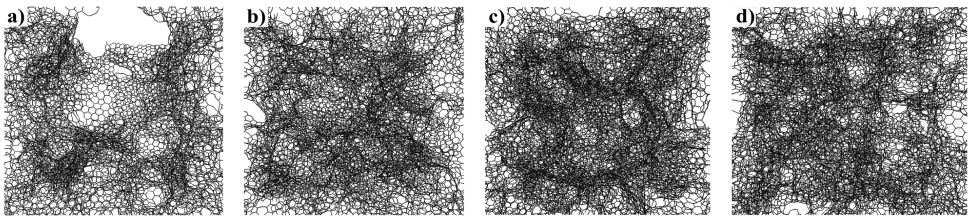

Figure 6: A similar part of a UC taken from four types GF with different porosity (a) 78% (b) 70% (c) 66% (d) 63%.

The variation of CTE relative to temperature is plotted for all types of GF samples, and the results are shown in Fig. 8. For sample types of GF at a temperature of 300 K, the CTE starts

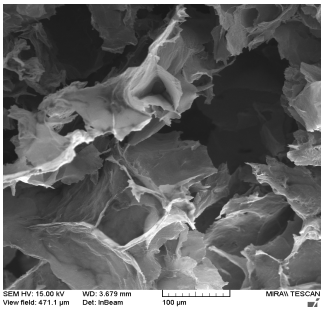

Figure 7: SEM image of a 3D GF with a matching topology studied in this work [21]

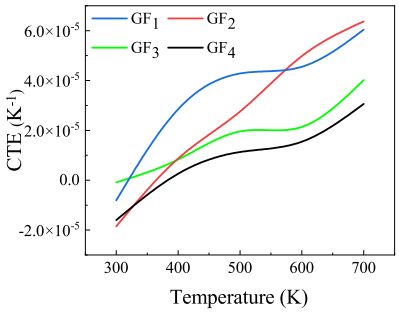

Figure 8: The CTE as a function of temperature for all groups of GFs.

Table 2: The thermoelastic properties for GFs by MD simulations.

Sample	T=300 K			T=400 K		
	SH* (J/g.K)	Heat capacity ($10^6\ J/m^3.K$)	CTE ($10^{-6}\ K^{-1}$)	SH* (J/g.K)	Heat capacity ($10^6\ J/m^3.K$)	CTE ($10^{-6}\ K^{-1}$)
GF_1	3.65	1.87	−8.08	3.78	1.94	33.3
GF_2	3.02	2.04	−18.5	3.08	2.09	8.69
GF_3	2.55	1.80	−5.13	2.69	1.90	2.62
GF_4	2.33	1.87	−1.31	2.35	1.89	0.89

* In this table, SH is used instead of specific heat.

with a negative value, which agrees with the experimental results of references [33, 34]. In fact, the CTE in GFs increases quickly at low temperatures, and gradually the rate decreases at higher temperatures. In general, up to 700 K, there are still many changes in CTE with temperature. This temperature is lower than the Debye temperature in graphene [35]. Increasing the temperature increases the motion of carbon atoms in the simulation box and thus increases the CTE. It is generally founded that as density increases, the CTE value decreases and tends to zero. The behavior of CTE for GFs at different densities and porosity is various and depends on the temperature and coordinate of carbon atoms. Further, the specific heat is calculated by computing the

system's internal energy for all types of GF samples. The values of the CTE, specific heat, and heat capacity at 300 K and 400 K are presented in Table 2. It can be deduced that the value of specific heat decreases for all samples with decreasing porosity. Additionally, it is clear that the heat capacity value for each sample depends on mass density. At 300 K, the first type GF with the lowest density has the maximum specific heat, and the fourth one with the highest density has the minimum specific heat. Also, rising temperature causes the value of specific heat increases for all samples. On the other hand, in the present numerical conditions, an attempt has been made to use the potential that is most consistent with the experimental conditions, but because quantum effects are not considered, it may cause a slight difference in the results with experimental conditions. The high specific heat of GFs shows that with low mass and high porosity, these materials are able to store high energy. Therefore, GFs are also used as batteries and energy storage in addition to structural and thermal applications.

In order to calculate the thermoelastic properties of the homogeneous GF/polymer composites by the micro-thermoelastic CUF model [27, 28], the heterogeneous UC information, including GFs and PDMS (Sylgard 184) matrix, is presented. Table 3 provides the values of Young modulus and Poisson ratio for the GF samples from the MD simulation in this study. The Young modulus for each GFs type in this study at temperatures between 300 K and 400 K is assumed to be constant, and the slight difference between them is ignored. Also, Poisson ratio for GFs is considered temperature-independent. The properties of the PDMS matrix are listed in Table 4 using references [36, 37, 38]. It should be noted that the PDMS is a cross-linked elastomer, and its behavior is in contrast with thermoplastic polymers. The modulus of PDMS increases with temperature because of the increased Brownian motion, leading to the stretched molecular segments tugging at their *anchor points* and taking a more likely coiled-up shape [39]. PDMS's density is 0.97 g/cm^3, and its Poisson ratio at all temperatures is 0.499.

Table 3: The elastic properties of GFs by MD simulations.

Material	Young modulus (GPa)	Poisson ratio
GF_1	4	0.27
GF_2	19	0.27
GF_3	23	0.29
GF_4	27	0.33

Table 4: Properties of PDMS matrix from references [36, 37, 38].

Temperature (K)	Young modulus (MPa)	Specific heat (J/g.K)	Heat capacity ($10^6\, J/m^3.K$)	CTE ($10^{-6}\, K^{-1}$)
300	1.4	1.45	1.40	285
400	2.2	1.65	1.60	275

Table 5 is presented to validate the MD method for GFs as well as the micro-thermoelastic CUF model for the effective properties of the composite used in this work. For this purpose, graphite and graphite/epoxy composite properties are calculated using the MD and micro-thermoelastic CUF models, respectively. The results obtained by numerical methods are compared to those obtained by the experimental procedure in reference [40]. These comparisons demonstrate that numerical methods provide accurate results.

Table 5: The comparison of the MD and the micro-thermoelastic CUF methods outputs with experimental results in ref. [40]

Material	Method	Young modulus (GPa)	Poisson ratio	Specific heat (J/g.K)	CTE ($10^{-6}\,K^{-1}$)
Graphite	Experimental	5	0.23	1.57	5
Graphite	MD	5.08	0.23	1.61	5.2
Epoxy	Experimental	2.6	0.35	1.92	82
Graphite/epoxy	Experimental	3	0.34	-	77
Graphite/epoxy	CUF	3.01	0.334	1.85	78

In the next step, GF/PDMS composites with four types of GF are investigated by the micro-thermoelastic CUF model at 300 K and 400 K. For all samples, GFs have a volume fraction of 8.1%. As reported in Table 6, at both 300 K and 400 K, the Young modulus of the resulting composite increased as the density of the GF samples increased. Poisson ratio also increased with decreasing percentage of reinforcement's porosity.

Table 6: The elastic properties of GF/PDMS composites by the micro-thermoelastic CUF model.

	T=300 K		T=400 K	
Composite	Young modulus (GPa)	Poisson ratio	Young modulus (GPa)	Poisson ratio
GF_1/PDMS	0.32	0.33	0.33	0.35
GF_2/PDMS	1.55	0.30	1.56	0.31
GF_3/PDMS	1.87	0.31	1.88	0.32
GF_4/PDMS	2.20	0.34	2.22	0.35

Likewise, Table 7 and 8 report the CTE and heat capacity of the resulting composites at 300 K and 400 K. Essentially, the CTE of composites increases with increasing porosity and temperature. To put it differently, increasing the number of atoms in the simulation box in dense GF samples diminishes the space of atom motion, resulting in a drop in CTE. At 300 K and 400 K, the composites reinforced with the fourth type of GFs have decreased CTE by 90% and 84%, respectively, compared to the PDMS, which had the most significant reduction. GFs have high stiffness and a very low CTE, which is very promising in applications requiring high dimensional stability. This feature causes the movement limitation of polymer chains and reduces the CTE of composites. Eventually, the CTE of the composites is validated with reference [5]. Alternatively, according to Eq 16 in c_v, effective heat capacity consists of two terms. The first term of this relationship depends on Young modulus, Poisson ratio, CTE, and geometry. In fact, this model concludes the effective CTE and heat capacity value by coupling the elastic and thermoelastic parameters. These effects cause the heat capacity of the GFs to have the opposite effect on the matrix and reduce the effective heat capacities in some samples. The second expression, which acts as the rule of mixtures, is that the effective heat capacity value is an average value between this parameter for the matrix and the fiber. In Table, 7 and 8, the parameters of effective heat capacity calculated by the two methods rule of the mixture and micro-thermoelastic CUF are presented at 300 K and 400 K. It is clear that the accuracy and impact of other parameters can be seen in the micro-thermoelastic method. Finally, the accuracy of these calculations is compared and confirmed with the output of the experimental measures[41].

Table 7: The thermoelastic properties for GF/PDMS composites at 300 K.

Composite	T=300 K		
	Heat capacity (CUF) ($10^6\ J/m^3.K$)	Heat capacity (rule of mixtures) ($10^6\ J/m^3.K$)	CTE ($10^{-6}\ K^{-1}$)
GF_1/PDMS	1.410	1.438	210
GF_2/PDMS	1.425	1.451	35
GF_3/PDMS	1.400	1.432	30
GF_4/PDMS	1.402	1.438	26

Table 8: The thermoelastic properties for GF/PDMS composites at 400 K.

Composite	T=400 K		
	Heat capacity (CUF) ($10^6\ J/m^3.K$)	Heat capacity (rule of mixtures) ($10^6\ J/m^3.K$)	CTE ($10^{-6}\ K^{-1}$)
GF_1/PDMS	1.56	1.627	240
GF_2/PDMS	1.58	1.639	86
GF_3/PDMS	1.54	1.624	62
GF_4/PDMS	1.55	1.623	42

5. Conclusions

In this study, the four types of GF simulated were examined in terms of CTE and specific heat relative to temperature. Calculating temperature-dependent properties improves the accuracy of the computations. A lower average dispersion in CTE was found for the last of the four GF groups with the maximal density and minimal porosity. Generally, GFs' CTE increased with temperature and porosity percentage. Calculating the specific heat of GFs uncovered that increasing the temperature also increases the specific heat. By a slight change in mass density and percentage of porosity at the nanometer scale, significant changes occur in the Young modulus of GF samples, resulting in their mechanical and thermoelastic properties acting differently from each other. It was found that at 300 K and 400 K, the maximum CTE belongs to the GF reinforced composite with the highest porosity percentage, and vice versa, the composite which is reinforced with dense GF has the minimum CTE. The high specific heat of GFs makes them an excellent energy storage material. It is worth noting that the specific heat of foams on the nanoscale depends, in addition to temperature, on other parameters such as the internal energy of the simulated box, which is proposed to be considered in future works. On the other hand, the effective heat capacity of composite depends not only on the heat capacity but also on the Young modulus, CTE, and geometry of its components. Finally, it was proved that the micro-thermoelastic CUF model used in this study is a very efficient and accurate model for calculating composites' thermoelastic properties using their constituents' properties. Furthermore, It was found that GFs with the highest porosity has the most significant specific surface area. The specific surface area decreases with decreasing porosity percentage. It is predicted that GF with random porosity and high specific surface area has the advantages such as fast ion diffusion rate and high electrochemical performance. For this reason, future work will be related to the computation of the electrochemical properties of these materials.

References

[1] S. Kabiri, D. N. Tran, T. Altalhi, D. Losic, Outstanding adsorption performance of graphene–carbon nanotube aerogels for continuous oil removal, Carbon 80 (2014) 523–533.

[2] H. Lin, S. Xu, X. Wang, N. Mei, Significantly reduced thermal diffusivity of free-standing two-layer graphene in graphene foam, Nanotechnology 24 (41) (2013) 415706.

[3] J. Jia, X. Sun, X. Lin, X. Shen, Y.-W. Mai, J.-K. Kim, Exceptional electrical conductivity and fracture resistance of 3d interconnected graphene foam/epoxy composites, ACS nano 8 (6) (2014) 5774–5783.

[4] M. Li, Y. Sun, H. Xiao, X. Hu, Y. Yue, High temperature dependence of thermal transport in graphene foam, Nanotechnology 26 (10) (2015) 105703.

[5] Y.-H. Zhao, Z.-K. Wu, S.-L. Bai, Study on thermal properties of graphene foam/graphene sheets filled polymer composites, Composites Part A: Applied Science and Manufacturing 72 (2015) 200–206.

[6] Y.-H. Zhao, Y.-F. Zhang, S.-L. Bai, X.-W. Yuan, Carbon fibre/graphene foam/polymer composites with enhanced mechanical and thermal properties, Composites Part B: Engineering 94 (2016) 102–108.

[7] Y.-F. Zhang, Y.-H. Zhao, S.-L. Bai, X. Yuan, Numerical simulation of thermal conductivity of graphene filled polymer composites, Composites Part B: Engineering 106 (2016) 324–331.

[8] A. Vahedi, M. H. S. Lahidjani, Tunable thermal conductivity along graphene/hexagonal boron-nitride polycrystalline heterostructures, The European Physical Journal Plus 132 (10) (2017) 1–7.

[9] U. Degirmenci, M. Kirca, Reverse non-equilibrium molecular dynamics simulations on the thermal conductivity of three-dimensional graphene nano-ribbon foams, Journal of Physics and Chemistry of Solids 136 (2020) 109130.

[10] H. Murakami, A. Toledano, A high-order mixture homogenization of bi-laminated composites, Applied Mechanics 57 (2) (1990) 388–397.

[11] C.-T. Sun, R. S. Vaidya, Prediction of composite properties from a representative volume element, Composites science and Technology 56 (2) (1996) 171–179.

[12] W. Yu, A unified theory for constitutive modeling of composites, Journal of Mechanics of Materials and Structures 11 (4) (2016) 379–411.

[13] E. Carrera, M. Cinefra, M. Petrolo, E. Zappino, Finite element analysis of structures through unified formulation, John Wiley & Sons, 2014.

[14] E. Carrera, M. Petrolo, Refined beam elements with only displacement variables and plate/shell capabilities, Meccanica 47 (3) (2012) 537–556.

[15] E. Carrera, S. Brischetto, A. Robaldo, Variable kinematic model for the analysis of functionally graded material plates, AIAA journal 46 (1) (2008) 194–203.

[16] E. Carrera, M. Maiaru, M. Petrolo, G. Giunta, A refined 1d element for the structural analysis of single and multiple fiber/matrix cells, Composite Structures 96 (2013) 455–468.

[17] M. Afzali, M. Farrokh, E. Carrera, Thermal buckling loads of rectangular fg plates with temperature-dependent properties using carrera unified formulation, Composite Structures (2022) 115787.

[18] S. Plimpton, Fast parallel algorithms for short-range molecular dynamics, Journal of computational physics 117 (1) (1995) 1–19.

[19] P. Hirel, Atomsk: A tool for manipulating and converting atomic data files, Computer Physics Communications 197 (2015) 212–219.

[20] S. J. Stuart, A. B. Tutein, J. A. Harrison, A reactive potential for hydrocarbons with intermolecular interactions, The Journal of chemical physics 112 (14) (2000) 6472–6486.

[21] S. Khosravani, M. H. Sadr, E. Carrera, A. Pagani, Synthesis, experimental testing and multi-scale modelling of graphene foam/epoxy composite, Mechanics of Advanced Materials and Structures (2022) 1–10.

[22] A. Stukowski, Visualization and analysis of atomistic simulation data with ovito–the open visualization tool, Modelling and Simulation in Materials Science and Engineering 18 (1) (2009) 015012.

[23] R. F. Sekerka, Thermal physics: thermodynamics and statistical mechanics for scientists and engineers, Elsevier, 2015.

[24] R. Zhou, X. Ma, H. Li, C. Sun, B. Bai, Specific heat capacity of confined water in extremely narrow graphene nanochannels, Frontiers in Energy Research (2021) 540.

[25] W. Yu, D. H. Hodges, Asymptotic approach for thermoelastic analysis of laminated composite plates, Journal of Engineering Mechanics 130 (5) (2004) 531–540.

[26] W. Yu, T. Tang, A variational asymptotic micromechanics model for predicting thermoelastic properties of heterogeneous materials, International Journal of Solids and Structures 44 (22-23) (2007) 7510–7525.

[27] A. G. De Miguel, A. Pagani, W. Yu, E. Carrera, Micromechanics of periodically heterogeneous materials using higher-order beam theories and the mechanics of structure genome, Composite Structures 180 (2017) 484–496.

[28] A. Sanchez-Majano, R. Masia, A. Pagani, E. Carrera, Microscale thermo-elastic analysis of composite materials by high order geometrically accurate finite elements, Submitted to Composite Structures (2022).

[29] E. Carrera, A. de Miguel, A. Pagani, Hierarchical theories of structures based on legendre polynomial expansions with finite element applications, International Journal of Mechanical Sciences 120 (2017) 286–300.
[30] A. Pagani, A. de Miguel, E. Carrera, Cross-sectional mapping for refined beam elements with applications to shell-like structures, Computational Mechanics 59 (6) (2017) 1031–1048.
[31] L. Sarkisov, R. Bueno-Perez, M. Sutharson, D. Fairen-Jimenez, Materials informatics with poreblazer v4. 0 and the csd mof database, Chemistry of Materials 32 (23) (2020) 9849–9867.
[32] A. Pedrielli, S. Taioli, G. Garberoglio, N. M. Pugno, Mechanical and thermal properties of graphene random nanofoams via molecular dynamics simulations, Carbon 132 (2018) 766–775.
[33] W. Bao, F. Miao, Z. Chen, H. Zhang, W. Jang, C. Dames, C. N. Lau, Controlled ripple texturing of suspended graphene and ultrathin graphite membranes, Nature nanotechnology 4 (9) (2009) 562–566.
[34] S. Mann, R. Kumar, V. Jindal, Negative thermal expansion of pure and doped graphene, RSC advances 7 (36) (2017) 22378–22387.
[35] T. Tohei, A. Kuwabara, F. Oba, I. Tanaka, Debye temperature and stiffness of carbon and boron nitride polymorphs from first principles calculations, Physical Review B 73 (6) (2006) 064304.
[36] F. Schneider, T. Fellner, J. Wilde, U. Wallrabe, Mechanical properties of silicones for mems, Journal of Micromechanics and Microengineering 18 (6) (2008) 065008.
[37] I. Johnston, D. McCluskey, C. Tan, M. Tracey, Mechanical characterization of bulk sylgard 184 for microfluidics and microengineering, Journal of Micromechanics and Microengineering 24 (3) (2014) 035017.
[38] G. Zhang, Y. Sun, B. Qian, H. Gao, D. Zuo, Experimental study on mechanical performance of polydimethylsiloxane (pdms) at various temperatures, Polymer Testing 90 (2020) 106670.
[39] D. W. Van Krevelen, K. Te Nijenhuis, Properties of polymers: their correlation with chemical structure; their numerical estimation and prediction from additive group contributions, Elsevier, 2009.
[40] S. Wang, M. Tambraparni, J. Qiu, J. Tipton, D. Dean, Thermal expansion of graphene composites, Macromolecules 42 (14) (2009) 5251–5255.
[41] Y.-H. Zhao, Z.-K. Wu, S.-L. Bai, Thermal resistance measurement of 3d graphene foam/polymer composite by laser flash analysis, International Journal of Heat and Mass Transfer 101 (2016) 470–475.